

Simulation of Crystal Sedimentation and Viscoplastic Behavior of Sedimented Equiaxed Mushy Zones

Andreas Ludwig¹ · Alexander Vakhrushev² · Menghuai Wu^{1,2} · Tobias Holzmann¹ · Abdellah Kharicha¹

Received: 29 June 2015 / Accepted: 18 August 2015 / Published online: 25 September 2015
© The Indian Institute of Metals - IIM 2015

Abstract During solidification of castings, equiaxed crystals that is formed sink downwards, sediment and form a packed bed. The behavior of separated moving crystals can be described by a submerged object approach, whereas the viscoplastic behavior of a semi-solid slurry follows a volume-averaged viscoplastic constitutive equation. In this work, a two-phase Eulerian–Eulerian volume-averaging approach is used to combine both flow regimes. The transition happens at a certain solid volume fraction, the so-called coherency limit. Starting with a uniform distribution of crystals at rest, sedimentation and packing of crystals are described. In addition, the material density of the crystal is assumed to increase on cooling and thus the domain shrinks which is also accounted for in this report. It is demonstrated how sensitive the model is, on the considered crystal diameters and on the assumed value for the coherency limits.

Keywords Equiaxed solidification · Visco-plasticity · Mushy zone · Sedimentation · Packed bed

List of symbols

α, β	Rheological function taken from [9]
$c_{p,\ell}, c_{p,s}$	Specific heat (J/kg/K)
C_e	Settling ratio (–)
d	Average crystal diameter (m)

g_ℓ, g_s	Volume fraction (–)
g_s^{pack}	Packing limit for hard spheres (–)
g_s^{cohe}	Coherency limit (–)
h_ℓ, h_s	Volume averaged enthalpy (J/kg)
H^*	Volume heat transfer coefficient (W/m ³ /K)
$H_{\ell s}$	Enthalpy exchange (J/m ³ /s)
I	Identity tensor (–)
k_ℓ, k_s	Heat conductivity (J/m ² /K)
K	Permeability (m ²)
K_v	Viscoplastic consistency (kg s ^{m–2} /m)
$K_{\ell s}$	Drag coefficient (kg/m ³ /s)
m	Strain rate sensitivity coefficient (–)
$M_{\ell s}$	Mass transfer (kg/m ³ /s)
p_ℓ, p_s	Pressure (N/m ²)
T_ℓ, T_s	Volume average temperature (K)
v_ℓ, v_s	Flow velocity (m/s)
$\dot{\varepsilon}_\ell, \dot{\varepsilon}_s$	Strain rate tensor (–)
$\dot{\varepsilon}_{eq}^s$	Equivalent strain rate (–)
μ_ℓ, μ_s	Viscosity (kg/m/s)
ρ_ℓ, ρ_s	Density (kg/m ³)
σ_ℓ, σ_s	Stress tensor (N/m ²)
τ_ℓ, τ_s	Deviatoric stress tensor (N/m ²)

1 Introduction

From 1936, researchers, such as Verö [1] and Bishop et al. [2] started to develop tensile testing equipments for testing mechanical properties of partially solidified alloys. Since the pioneering work of Flemings and colleagues [3, 4] it is well known that during solidification when the solid volume fraction exceeds a certain limit, the semi-solid metal slurry shows viscoplastic flow behavior. This behavior is

✉ Andreas Ludwig
ludwig@unileoben.ac.at

¹ Chair for Modeling and Simulation of Metallurgical Processes, Montanuniversitaet Leoben, Leoben, Austria

² Christian-Doppler Laboratory for Advanced Process Simulation of Solidification & Melting, Montanuniversitaet Leoben, Leoben, Austria

generally expressed by a stress-strain rate relation of Norton–Hoff type that is often used to describe the hot deformation of alloys in the fully solid-state [5] as

$$\sigma = \sqrt{3}K_v \left(\sqrt{3}\dot{\epsilon} \right)^m, \quad (1)$$

where σ represents the stress tensor, $\dot{\epsilon}$ the strain-rate tensor, K_v the viscoplastic consistency and m the strain-rate sensitivity. Dahle et al. [6–8] reported results of measurements of the development of shear strength during solidification of some common aluminum alloys as a function of morphology and fraction solid. Suéry et al. further investigated the behavior of semi-solid metal slurries and suggested several macroscopic approaches for modelling its rheological behavior [9–13]. Their models are based on continuum mechanics and mixture theory, and suggest constitutive equations for the compressible viscoplastic solid phase. The semi-solid material is assimilated as porous media saturated with liquid, which has been characterized by the supplementary internal parameters which represent the phase volume fractions. Therefore, the viscoplastic deformation of the solid skeleton is no longer incompressible, but induces volume variations, and consequently liquid flow through the solid skeleton. The stress field in this case is then composed of the solid phase stress in the solid matrix and the interstitial pressure in the liquid.

Although some asymmetry between tension and compression was reported [11, 12], in the present paper we refer to the symmetrical model by Nguyen–Favier–Suéry (herein called as NFS-approach) alone, [9] in which the effective macroscopic solid stress tensor σ^s is related to the volume averaged strain-rate tensor $\dot{\epsilon}_s$ by

$$\sigma^s = 2\mu_s^{\text{app}} \left(\alpha \cdot \dot{\epsilon}_s - \beta \cdot \frac{1}{3} \text{tr}(\dot{\epsilon}_s) \mathbf{I} \right), \quad (2)$$

where α and β are empirical functions of the solid volume fraction and μ_s^{app} is the apparent solid viscosity given by

$$\mu_s^{\text{app}} = \frac{\sigma_{eq}}{\dot{\epsilon}_{eq}^s} = 3K_v \left(\sqrt{3}\dot{\epsilon}_{eq}^s \right)^{m-1}, \quad (3)$$

with σ_{eq} being the von Mises equivalent stress scalar and $\dot{\epsilon}_{eq}^s$ the von Mises equivalent strain-rate scalar. It is to be noted that Eq. (3) include the Norton–Hoff law, Eq. (1). It is to be noted further that when $\alpha = 1$ and $\beta = 1$, Eq. (2) is reduced to the general relation between the strain-rate and the deviatoric stress tensor. According to [9] the two empirical rheological functions are defined for $g_s > 0.55$ as

$$\alpha(g_s) = \frac{1}{3}g_s^{6.47}, \quad (4)$$

$$\beta(g_s) = \frac{1}{3}g_s^{6.47} - \frac{1}{0.054} \cdot \left[\frac{1}{g_s^{6.94}} - 1 \right]^{-1}. \quad (5)$$

Bullet et al. [14, 15] used the above NFS-approach for the volume-averaged version of the effective macroscopic stress tensor of the solid phase in the mushy zone of a continuous casting of steel. In this paper, they solved the volume-averaged mass and momentum conservation equations for the liquid and the solid phases assuming a solid volume fraction of more than 0.55. At this point it is important to note that the effective macroscopic solid stress tensor σ^s and the volume-averaged deviatoric solid stress tensor τ_s are related by

$$\sigma^s = g_s \tau_s, \quad (6)$$

(see Eq. (11) in [9]) and that Eq. (2) is the sum of the deviatoric solid stress tensor and the solid pressure [14, 15] (which is in fact assumed to be approximately the liquid pressure at the solid/liquid interface).

Below the solid fraction of the coherency limit, where the equiaxed crystals are relatively free to move, their motion can be described by either the equation of motion for a single grain or by a volume-averaged momentum conservation equation for the solid phase. In [16–18], a single-phase, one-domain macroscopic model has been used to study binary alloy solidification with moving equiaxed solid phase. Herein, the equation of motion of single grain is solved using an effective viscosity for the solid/liquid mixture. The presence of the equiaxed crystals is accounted for in the momentum conservation equation of the mixture. In [19–36], the volume-averaged momentum conservation equation for the liquid and the solid phase is solved describing the viscosity of the solid/liquid mixture [37],

$$\mu_{mix} = \mu_l \cdot \left(1 - \frac{g_s}{g_s^c} \right)^{-2.5 \cdot g_s^c}, \quad (7)$$

with g_s^c representing a critical solid volume fraction above which the equiaxed crystals are supposed to merge to form a rigid solid structure. For the larger solid volume fractions, Eq. (7) predicts an increasing viscosity of the solid/liquid mixture till it approaches infinity for $g_s \rightarrow g_s^c$. Assuming the validity of a mixing rule for viscosity [38], $\mu_s = g_l \mu_l + g_s \mu_s$, Eq. (7) can be used to derive an expression for the effective viscosity of the solid phase as

$$\mu_s = \frac{\mu_l}{g_s} \left(\left[1 - \frac{g_s}{g_s^c} \right]^{-2.5 g_s^c} - (1 - g_s) \right). \quad (8)$$

In [19–36], the classical packing limit for equal diameter hard spheres, $g_s^{\text{pack}} = 0.637$, was taken for g_s^c .

So, for small solid volume fraction the motion of equiaxed crystals can be described by volume-averaged momentum conservation equation for the solid phase assuming an effective solid viscosity according to Eq. (8) and for large solid volume fraction the viscoplastic behavior of the semi-solid slurry can be described by a volume-averaged momentum conservation equation for the solid phase using the NFS-approach, Eq. (2). It is obvious that a combination of both approaches can be used to describe the motion of the solid phase over the whole range of solid volume fraction from few equiaxed grains floating in the liquid to a dense coherent dendritic network which is deforming and allowing the residual melt to flow through.

In the present paper, we have combined the two approaches and discussed especially assumptions necessary for the transition from the effective solid viscosity to the viscoplastic regime. In order to focus on these details we did not consider neither any nucleation nor solidification. We rather investigated the sedimentation of (globular) equiaxed crystals till they form a coherent backed bed, which then continue to deform by further draining of liquid and thermal shrinkage of the solid phase. The present report is the second paper of the authors on that topic [39].

2 Model Description

The volume-averaged approach used in this paper assumes that at any point in space and time the amount of the two phases, liquid and solid, can be represented by the corresponding volume fractions, g_l and g_s , whereby the sum adds up to one. For both phases the volume-averaged mass, momentum and enthalpy conservation equations according to Table 1 are solved. As mentioned before, nucleation and solidification are not considered. We rather assume that a certain volume fraction of solid with a given crystal diameter is initially equally distributed within the domain and that the material density of these crystals is larger than that of the liquid. As we consider gravity action, the crystals start to sediment downwards. This sedimentation motion is described by solving the volume-averaged momentum conservation equation for the solid, Eq. (13), assuming an effective solid viscosity according to Eq. (8) and that the solid and the liquid phase share the same pressure field, p . In this flow regime, the momentum exchange between liquid and solid due to drag is described by the so-called submerged object approach [40] according to the first equation in Eq. (22).

If sedimentation continues, the amount of crystals in the lower part of the domain increases and thus the limit of the validity range of the effective solid viscosity and the submerged object approach is reached. On further increasing solid volume fraction, the crystals form a coherent solid

network which may allow the residual liquid to flow through. For this regime, the model for the momentum exchange between solid and liquid due to drag is changed to the porous medium approach where the coherent network reveals a certain flow permeability. In this paper we have used a Kozeny–Carman-type permeability according to the second equation of Eq. (22). For the divergence of the effective macroscopic solid stress tensor we have used the NFS-approach according to Eq. (17).

2.1 Transition Between Flow Regimes

As in nature the submerged object flow regime changes continuously into the porous medium flow regimes, the two governing momentum conservation equations for the solid phase should merge when the transition occurs. Mathematically the two regimes differ by (i) the momentum exchange term between liquid and solid [Eq. (22)] and (ii) the expression of the effective macroscopic solid stress tensor [Eqs. (15) and (17)]. Due to two different underlying physics, both differences should merge at the transition separately.

In order to ensure a smooth transition for the momentum exchange term between liquid and solid, we have chosen a prefactor for the flow permeability of the solid network such that the drag terms for the submerged object and the porous medium approaches are equal at the transition point [Eq. (22)]. Although this choice might be artificial, it is justified by the fact that the exact value of the permeability of a dendritic networks is seldom known precisely. As discussed in [41], literature values of mushy zone permeabilities especially at high solid volume fraction can easily vary by one–two orders of magnitude or even more. On the other hand, it is also conceivable that the settling ratio, C_s , might change when the amount of crystals become so dense that collective flow phenomenon occur. Here, detailed knowledge about the physics involved, is missing. In the present paper, we assume that the transition from the submerged object to the porous medium flow regime happens at the coherency limit, g_s^{cohe} .

Merging the expressions of the effective macroscopic solid stress tensor is even more difficult. The effective viscosity approach considers a case where the solid/liquid mixture might reveal an infinite viscosity for $g_s \rightarrow g_s^c$. This is in principle not consistent with the NFS-approach, where the solid/liquid mixture reveals viscoplastic flow behavior as it does in reality. We thus assume that in the transition region the NFS-approach describes the reality better and so in this region the effective viscosity approach must be seen only as rough approximation. It is to be noted that in the present work we use for the infinite limit of the effective viscosity of the solid, the packing limit for equal diameter hard spheres, $g_s^c = g_s^{\text{pack}} = 0.637$, whereas for the

Table 1 List of conservation equations

Mass conservation	
$\frac{\partial}{\partial t}(g_\ell \rho_\ell) + \nabla \cdot (g_\ell \rho_\ell \mathbf{v}_\ell) = 0$	(9)
$\frac{\partial}{\partial t}(g_s \rho_s) + \nabla \cdot (g_s \rho_s \mathbf{v}_s) = 0$	(11)
Momentum conservation	
$\frac{\partial}{\partial t}(g_\ell \rho_\ell \mathbf{v}_\ell) + \nabla \cdot (g_\ell \rho_\ell \mathbf{v}_\ell \mathbf{v}_\ell) = -g_\ell \nabla p + \nabla \cdot g_\ell \boldsymbol{\tau}_\ell$	(12)
$+ g_\ell \rho_\ell \mathbf{g} - K_{\ell s}(\mathbf{v}_\ell - \mathbf{v}_s)$	
$\frac{\partial}{\partial t}(g_s \rho_s \mathbf{v}_s) + \nabla \cdot (g_s \rho_s \mathbf{v}_s \mathbf{v}_s) = -g_s \nabla p + \nabla \cdot g_s \boldsymbol{\tau}_s$	(13)
$+ g_s \rho_s \mathbf{g} + K_{\ell s}(\mathbf{v}_\ell - \mathbf{v}_s)$	
$\boldsymbol{\tau}_\ell = 2\mu_\ell(\dot{\mathbf{e}}_\ell - \frac{1}{3}\text{tr}(\dot{\mathbf{e}}_\ell)\mathbf{I})$; $\dot{\mathbf{e}}_\ell = \frac{1}{2}(\nabla \mathbf{v}_\ell + (\nabla \mathbf{v}_\ell)^T)$;	(14)
$\text{tr}(\dot{\mathbf{e}}_\ell) = \nabla \cdot \mathbf{v}_\ell$	
For $g_s \leq g_s^{\text{cohe}}$	
$\mathbf{v}_s = 2\mu_s(\dot{\mathbf{e}}_s - \frac{1}{3}\text{tr}(\dot{\mathbf{e}}_s)\mathbf{I})$; $\dot{\mathbf{e}}_s = \frac{1}{2}(\nabla \mathbf{v}_s + (\nabla \mathbf{v}_s)^T)$	(15)
$\text{tr}(\dot{\mathbf{e}}_s) = \nabla \cdot \mathbf{v}_s$	
With $\mu_s = \frac{\mu_\ell}{g_s} \left(\left(1 - \frac{g_s}{g_s^{\text{cohe}}} \right)^{-2.5g_s^{\text{cohe}}} - (1 - g_s) \right)$	(16)
For $g_s > g_s^{\text{cohe}}$	
$g_s \boldsymbol{\tau}_s = 2\mu_s^{\text{app}}(\alpha \cdot \dot{\mathbf{e}}_s - \beta \cdot \frac{1}{3}\text{tr}(\dot{\mathbf{e}}_s)\mathbf{I})$	(17)
With $\mu_s^{\text{app}} = 3K_v(\sqrt{3}\dot{\mathbf{e}}_{eq})^{m-1}$ and $\dot{\mathbf{e}}_{eq}^2 = 2\alpha \sum_{ij} \dot{e}_{s,ij} \dot{e}_{s,ij}$	(18)
$- 6\beta \cdot \left(\frac{1}{3} \text{tr}(\dot{\mathbf{e}}_s) \right)$	
Enthalpy conservation	
$\frac{\partial}{\partial t}(g_\ell \rho_\ell h_\ell) + \nabla \cdot (g_\ell \rho_\ell \mathbf{v}_\ell h_\ell) = \nabla \cdot (g_\ell k_\ell \nabla T_\ell) - H^*(T_\ell - T_s)$	(19)
$\frac{\partial}{\partial t}(g_s \rho_s h_s) + \nabla \cdot (g_s \rho_s \mathbf{v}_s h_s) = \nabla \cdot (g_s k_s \nabla T_s) + H^*(T_\ell - T_s)$	(20)
$h_\ell = \int c_{p,\ell} dT + h_\ell^{\text{ref}}$ and $h_s = \int c_{p,s} dT + h_s^{\text{ref}}$ and	(21)
$L = h_\ell^{\text{ref}} - h_s^{\text{ref}}$	

Symbols are defined in the List of Symbols

coherency limit we looked at two different cases. Neglecting the strain-rate dependence at the coherency limit by setting the strain rate sensitivity coefficient equal to one, $m = 1$, we ensure a smooth transition at the coherency limit g_s^{cohe} by estimating the viscoplastic consistency, K_v , from equalizing the prefactors of the strain-rate terms in Eqs. (15) and (17) as

$$3\alpha_s^{\text{cohe}} K_v = g_s^{\text{cohe}} \mu_s^{\text{cohe}}. \quad (10)$$

The strain rate sensitivity is switched on by changing m within a solid volume fraction interval of 2 % from 1 to its assumed value of $m = 0.139$.

For Case A, g_s^{cohe} is selected to be similar but a little smaller than $g_s^c = g_s^{\text{pack}} = 0.637$. We chose, $g_s^{\text{cohe}} = g_s^c - 10^{-4}$. This choice is made to avoid an infinite effective solid viscosity at the coherency limit, μ_s^{cohe} , which occur according to Eq. (16). With that, we got $K_v = 7668 \text{ kg/s/m}$ for the viscoplastic consistency which makes the apparent viscosity quite high and the packed bed kind of rigid. For Case B, we assume for the coherency limit the minimum value used for the evaluation of the measurement in [9] that's $g_s^{\text{cohe}} = 0.57$. With that choice and applying the condition Eq. (10), we got $K_v = 19 \text{ kg/s/m}$ for the viscoplastic consistency in Case B. This low

Table 2 Exchange terms as used in Eqs. (11)–(20)

Momentum exchange	
$K_{\ell s} = 18g_\ell^2 \frac{\mu_\ell g_s C_e}{d^2}$ for $g_s < g_s^{\text{cohe}}$ with $C_e = 10 \frac{g_s^3}{g_\ell^3}$	(22)
$= g_\ell^2 \frac{\mu_\ell}{K}$ for $g_s \geq g_s^{\text{cohe}}$ with $K = d^2 \frac{1}{180} 10 \frac{g_\ell^3}{g_s^2}$	
Enthalpy exchange	
$H^* = 10^8 \text{ W/m}^3/\text{K}$	(23)

value for K_v results in a relatively low apparent viscosity and so an enhanced fluidity of the packed bed. Please note that the exact value of K_v is alloy dependent and is often missing. It will be a future task to evaluate experimental results on semi-solids described in literature in order to get suitable values for the viscoplastic consistency and so, with the transition conditions Eq. (10) can be indirectly used to obtain the coherency limit, g_s^{cohe} (Table 2).

2.2 Calculation of Domain Deformations

In order to allow the density of the two phases to increase on cooling, we account for local volume changes. This is done based on the information of the mass fluxes at the domain boundaries required to compensate the volume shrinkage. For that a compressible mixture sub-model is applied with the opened domain boundaries as opposed to the closed one for the multiphase model. The boundary displacements are calculated by interpolating the velocity at the face centers to the boundary points. After the boundary points are moved, the internal mesh is smoothed by solving a Laplace equation for the cell centers to maintain the mesh quality. This procedure is done for each time step and the coupling between mesh motion and flow calculation is repeated until the zero boundary fluxes are reached. Further details of the shrinkage model and its implementation can be found in [39].

2.3 Initial and Boundary Conditions

As simple case, we have considered initially a rectangular domain (Fig. 1) with adiabatic walls except at the bottom where a certain heat extraction is assumed. As flow boundary conditions, the nonslip conditions is applied for the liquid and the slip condition for the solid. An initially homogenous distribution of a stationary solid/liquid mixture with a given crystal diameter and solid volume fraction is assumed to fill the domain. As material, we consider a “binary” steel (Fe–C alloy) with properties as given in Table 3.

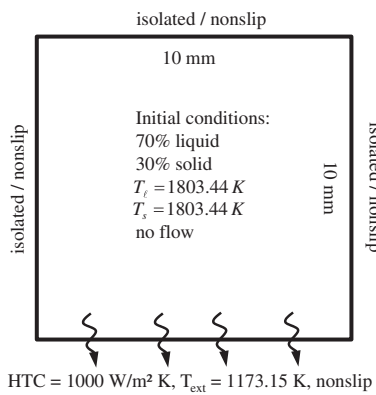


Fig. 1 Domain with the boundary and initial conditions

3 Results and Discussion

First the dependence of the average crystal diameter on the sedimentation and the formation of a packed bed is investigated. For Case A we have varied the diameter by $d = 0.125, 0.25, 0.5, 0.75$ and 1 mm , respectively. Note that an increasing crystal size has two effects: first, the drag between crystals and melt gets smaller with larger diameter, and thus sedimentation happens faster. On the other hand, according to the chosen transition condition in Eq. (22), the permeability of the packed bed increases with the crystal diameter. Therefore, the residual melt can more easily flow through the sedimented bed. In Fig. 2 the temporal evolution of the vertical component of the solid phase velocity averaged of the domain, \bar{v}_s^z , is shown together with figures that show the distribution of solid fraction for a few characteristic points with times for all five selected crystal diameters.

For the smallest diameter investigated ($d = 0.125\text{ mm}$, Fig. 2a) the settling process is very even and slow. This is the result of the high drag between the phases. The averaged settling velocity changes smoothly during the whole settling process. When the crystals are finally packed only a slightly distorted packed bed is formed that reveals some minor channels. For crystals with a diameter of $d = 0.125\text{ mm}$ a dense packed bed has already formed after $t = 45\text{ s}$. At this point in time the averaged settling

velocity reveals a minimum. Figure 2b shows that two symmetrically localized channels with a higher liquid fraction has formed. Together with additional smaller channels the two initial channels become stronger. It is important to mention that these channels collapse from time to time, releasing the entrapped liquid. That explains the increase in the domain-averaged settling velocity after the occurrence of the minimum and also its slight oscillation.

In the case of the half-millimeter crystals ($d = 0.5\text{ mm}$, Fig. 2c) a dense packed bed is observed already at $t = 12\text{ s}$. Now if compared to the previous cases, instead of two dominating vertical channels a series of slightly inclined channels combined with the vertical ones forms. This tendency continues with the $d = 0.75\text{ mm}$ crystals (Fig. 2d) where the dense packed bed and the minimum in the settling velocity occurs rather quickly at $t = 6\text{ s}$. Note that with larger grain diameter, and thus larger mush permeability, the liquid can drain more easily so that the amount of solid fraction in the packed bed at $t = 190\text{ s}$ is higher (denser packed bed) whereby the thickness of the packed bed is smaller.

The interesting change is observed for the biggest diameter investigated in this study ($d = 1\text{ mm}$, Fig. 2e). The settling velocity decreases due to the fact that the crystals are packed very fast to the stable structure which resists to the further settling of the solid phase. The final stage of the smooth separation of the phases (minimum of \bar{v}_s^z) is postponed to $t = 13\text{ s}$ (if compared to $t = 6\text{ s}$ in the previous case). A structure of the packed crystals remains stable in the center of the domain, whereby the two inclined channels are formed left and right to it, initiating a collapse of the packed bed and corresponding drain of liquid.

In Fig. 3 the time-averaged value of \bar{v}_s^z for the discussed five cases is shown. The time-averaged settling velocity increases first with the increasing crystal diameter. This is in accordance to the drag law, Eq. (22). However, for crystals with $d = 0.5\text{ mm}$ and larger, the increase becomes minor and even changes into a decrease for $d = 1\text{ mm}$. This can be explained by the packed crystals structure formation, which resists a further sinking of the solid

Table 3 Thermodynamic and physical properties

Properties	Symbols	Units	Quantities	References
Density (liquid)	$\rho_{\ell(T)}$	kg/m^3	$6990 - 1.07 \times 10^{-4} \frac{T_0-T}{K}$	[42]
Density (solid)	$\rho_{s(T)}$	kg/m^3	$7140 - 63 \times 10^{-6} \frac{T_0-T}{K}$	[43]
Specific heat of ℓ and s	$c_{p,\ell}, c_{p,s}$	$\text{J}/\text{kg}/\text{K}$	500	[42]
Thermal conductivity of ℓ and s	k_ℓ, k_s	$\text{W}/\text{m}/\text{K}$	34	[42]
Liquid viscosity	ℓ	$\text{kg}/\text{m}/\text{s}$	4.2×10^{-3}	[42]
Strain rate sensitivity coefficient	m_v	—	0.139	[44]

Fig. 2 Domain-averaged settling velocity v_s^z as function of time for different crystal diameters d : **a** 0.125 mm, **b** 0.25 mm, **c** 0.5 mm, **d** 0.75 mm, and **e** 1 mm. The insets show the distribution of solid fraction with dark blue for 0 %, bright blue for 30 % and dark red for 100 %. The yellow channels have around 60 % solid fraction

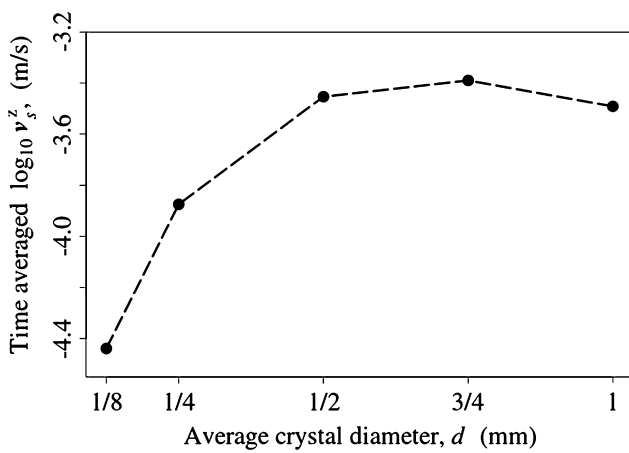
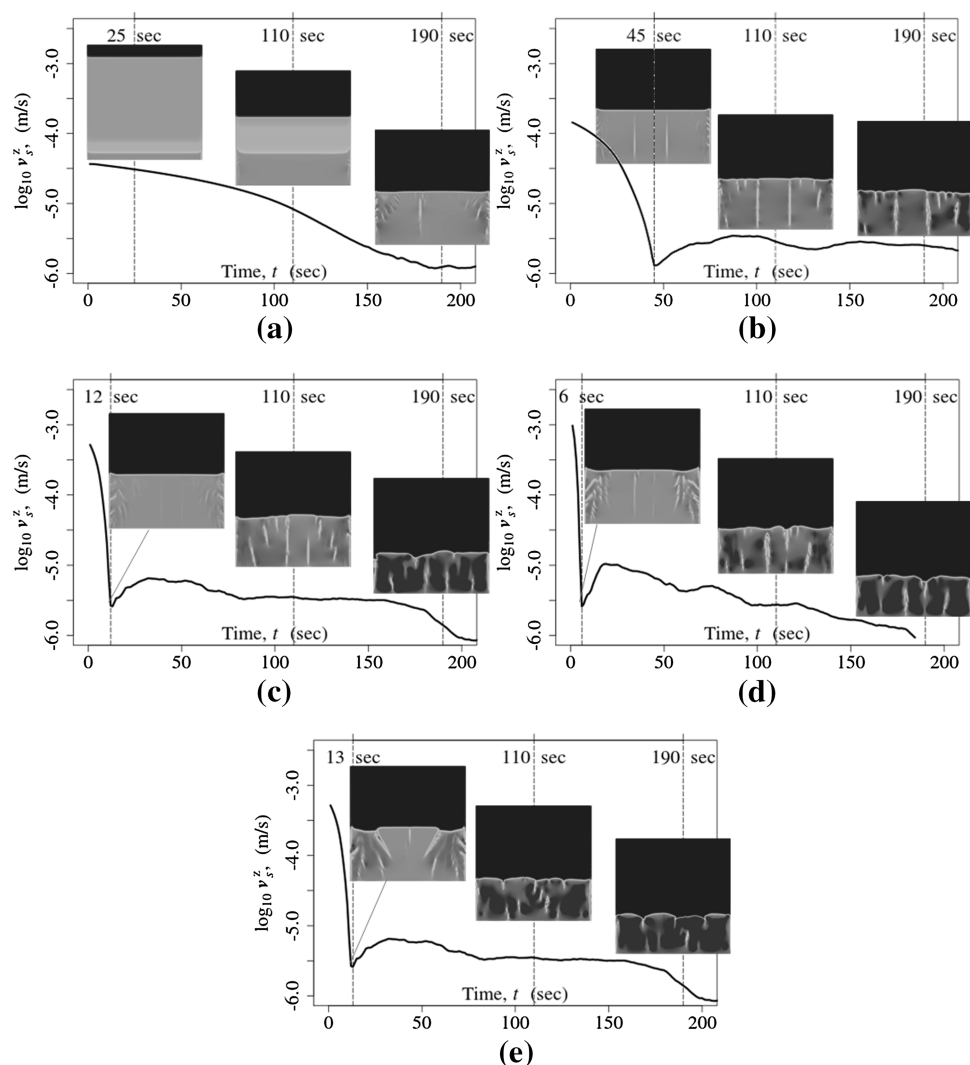


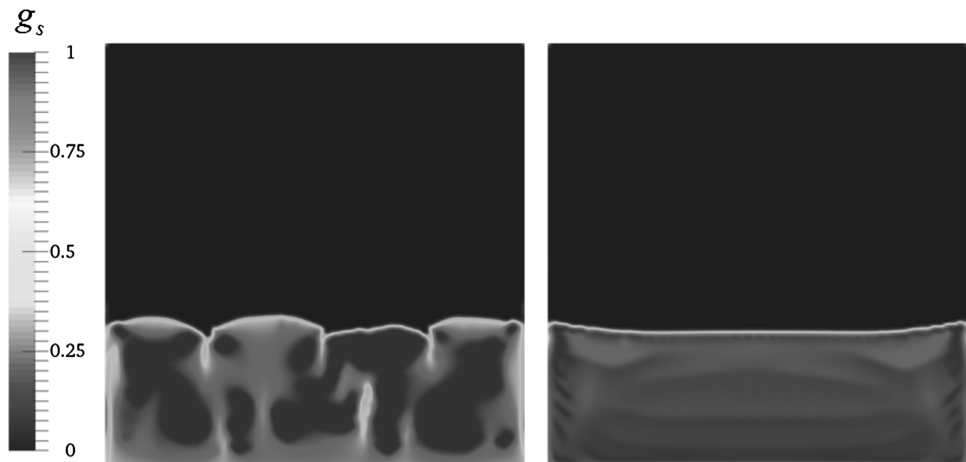
Fig. 3 Time-averaged value of v_s^z as function of crystal diameter

phase. It should be noticed that a complex channel system formation and the liquid drainage makes the character of the process nonlinear.

In the second part of this study, we have compare the two cases, A and B, where the assumed coherency limit is changed from $g_s^{\text{cohe}} = 0.637$ (Case A) to $g_s^{\text{cohe}} = 0.57$ (Case B) both with an average crystal diameter of $d = 1$ mm. Figure 4 shows the solid fraction distribution of both cases at $t = 200$ s. Obviously, the solid is much more uniformly distributed in Case B. As stated above, a smaller coherency limit results in a much smaller viscoplastic consistency ($K_v = 19$ kg/s/m compared to $K_v = 7668$ kg/s/m) and thus the apparent solid viscosity of Case B is much smaller. That's why the strain-rate dependent flow of solid is easier in Case B and so an uneven solid fraction distribution smears out faster.

It is also worth mentioning, that in Case A, areas of nearly 100 % solid fraction have formed side by side with channels that reveal only 60 % or less. The higher the solid fraction the more complicate is it to move the slurry. Therefore, the solid fraction distribution shown in Fig. 4a is changing only quite slowly and it will take much longer

Fig. 4 Solid fraction distribution at $t = 200$ s for Case A ($g_s^{\text{cohe}} = 0.637$) (left) and for Case B ($g_s^{\text{cohe}} = 0.57$) (right) both with $d = 1$ mm



time to finally produce a uniformly distributed packed bed. In contrast to that, Case B reveals a quite uniform solid fraction distribution of around 95 %. Here, the packing is nearly finished.

4 Conclusions

Based on a combined Eulerian–Eulerian volume-averaged approach the sedimentation of crystals was modelled with a submerge object approach and the strain-rate dependent behavior of the packed bed with a volume-averaged viscoplastic approach. Special emphasis was put on the transition between two models. The results showed that the behavior of the forming packed bed depended strongly on the assumed crystal diameter and the value of the coherency limit. For a small crystal diameter and a low coherency limit, packing was smooth and quite uniform. In contrast, for a larger crystal diameter and a large coherency limit, packing was uneven and channels of high liquid fraction formed within the packed bed, which then tended to collapse and allowed the residual liquid to drain. Future work will focus on measured material parameters (like viscoplastic consistency or the strain-rate sensitivity) and the implication that these measured parameters might have on sedimentation and packing. Nucleation and solidification should also be added.

Acknowledgments This work was financially supported by the FWF Austrian Science Fund (P22614-N22), FFG Bridge Early Stage (No. 3893791), and the Austrian Federal Ministry of Economy, Family and Youth and the National Foundation for Research, Technology and Development within the framework of the Christian Doppler Laboratory for Advanced Process Simulation of Solidification and Melting.

References

1. Verö J, *Met Ind* **48** (1936) 431.
2. Bishop H F, Ackerlind C G, and Pellini W S, *AFS Trans* **65** (1957) 247.
3. Laxmanan V, and Flemings M C, *Met Trans A* **11** (1980) 1927.
4. Suery M, and Flemings M C, *Met Trans A* **13** (1982) 1809.
5. Flemings M C, *Met Trans B* **22** (1991) 957.
6. Dahle A K, and Arnberg L, *Acta Mater* **45** (1997) 547.
7. Dahle A K, and StJohn D H, *Acta Mater* **47** (1998) 31.
8. Dahle A K, StJohn D H, Thevik H J, and Arnberg L, *Metall Mater Trans B* **30** (1999) 287.
9. Nguyen T G, Favier D, and Suery M, *Int J Plast* **10** (1994) 663.
10. Martin C L, Brown S B, Favier D, and Suery M, *Mater Sci Eng* **202** (1995) 13.
11. Martin C L, Favier D, and Suery M, *Int J Plast* **13** (1997) 237.
12. Martin C L, Favier D, and Suery M, *Int J Plast* **15** (1999) 981.
13. Ludwig O, Drezet J-M, Martin C L, and Suery M, *Metall Mater Trans A* **36** (2005) 1525.
14. Fachinotti V D, Le Corre S, Triolet N, Bobadilla M, and Bellet M, *Int J Numer Methods Eng* **67** (2006) 1341.
15. Bellet M, in *9th International Conference on Numerical Methods in Industrial Forming Processes*, (eds) Cesar de Sa J M A, and Santos A D, American Institute of Physics, Porto (2007), p 1369.
16. Kumar A, and Dutta P, *Int J Heat Mass Transf* **48** (2005) 3674.
17. Kumar A, Walker M J, Sundarraj S, and Dutta P, *Metall Mater Trans B* **42** (2011) 825.
18. Kumar A, Walker M J, Sundarraj S, and Dutta P, *Metall Mater Trans B* **42** (2011) 783.
19. Ludwig A, and Wu M, *Metall Mater Trans A* **33** (2002) 3673.
20. Wu M, Ludwig A, Bührig-Polaczek A, Fehlbier M, and Sahm P R, *Int J Heat Mass Transf* **46** (2003) 2819.
21. Wu M, and Ludwig A, *Mater Sci Eng A* **413–414** (2005) 192.
22. Wu M, Ludwig A, and Luo J, *Mater Sci Forum* **475–479** (2005) 2725.
23. Ludwig A, and Wu M, *Mater Sci Eng A* **413–414** (2005) 109.
24. Wang T, Wu M, Ludwig A, Abondano M, Pustal B, and Bührig-Polaczek A, *Int J Cast Met Res* **18** (2005) 221.
25. Wu M, and Ludwig A, *Metall Mater Trans A* **37** (2006) 1613.
26. Wu M, and Ludwig A, in *11th International Conference on Modeling of Casting, Welding and Advanced Solidification Processes (MCWASP XI)*, Opio, France, (eds) Gandin C-A, and Bellet M (2006), p 291.

27. Wang T M, Lin T J, Cao Z Q, Jin J Z, Grimmig T, Bührig-Polaczek A, Wu M, and Ludwig A, *Acta Metall Sin* **42** (2006) 591.
28. Wu M, and Ludwig A, *Metall Mater Trans A* **38** (2007) 1465.
29. Wu M, and Ludwig A, *Acta Mater* **57** (2009) 5621.
30. Wu M, and Ludwig A, *Acta Mater* **57** (2009) 5632.
31. Wu M, Fjeld A, and Ludwig A, *Comput Mater Sci* **50** (2010) 32.
32. Wu M, Ludwig A, and Fjeld A, *Comput Mater Sci* **50** (2010) 43.
33. Kharicha A, Stefan-Kharicha M, Ludwig A, and Wu M, *IOP Conf Ser Mater Sci Eng* **33** (2012) 012042.
34. Wu M, Ahmadein M, Kharicha A, Ludwig A, Li J, and Schumacher P, *IOP Conf Ser Mater Sci Eng* **33** (2012) 012075.
35. Wu M, Li J, Kharicha A, Ludwig A, in *1st International Conference on Ingot Casting, Rolling and Forging* (2012), p 1.
36. Li J, Wu M, Ludwig A, and Kharicha A, *Int J Heat Mass Transf* **72** (2014) 668.
37. Ishii M, and Zuber N, *AIChE J* **25** (1979) 843.
38. Ni J, and Beckermann C, *Metall Trans B* **22** (1991) 349.
39. Ludwig A, Vakhrushev A, Holzmann T, Wu M, and Kharicha A, *IOP Conf Ser Mater Sci Eng* **84** (2015) 012102.
40. Wang C Y, Ahuja S, Beckermann C, and De Groh III H C, *Metall Mater Trans B* **26** (1995) 111.
41. Ludwig A, Kharicha A, Hödlz C, Domitner J, Wu M, and Puszta T, *Eng Anal Bound Elem* **45** (2014) 29.
42. Combeau H, Založník M, Hans S, and Richy P E, *Metall Mater Trans B* **40** (2009) 289.
43. Wu M, Li J, Ludwig A, and Kharicha A, *Comput Mater Sci* **79** (2013) 830.
44. Kozlowski P F, Thomas B G, Azzi J A, and Wang H, *Metall Mater Trans A* **23** (1992) 903.